Supplement of Atmos. Chem. Phys., 26, 8893–8912, 2026
https://doi.org/10.5194/acp-26-8893-2026-supplement

Atmospheric Chemistry and Physics
Open Access

Supplement of

Aerosol Size Distribution and New Particle Formation in High Mountain Environments: A Comparative Study at Monte Cimone and Jungfraujoch GAW Stations

Martina Mazzini et al.

Correspondence to: Martina Mazzini (m.mazzini@isac.cnr.it)

S1 Data Availability

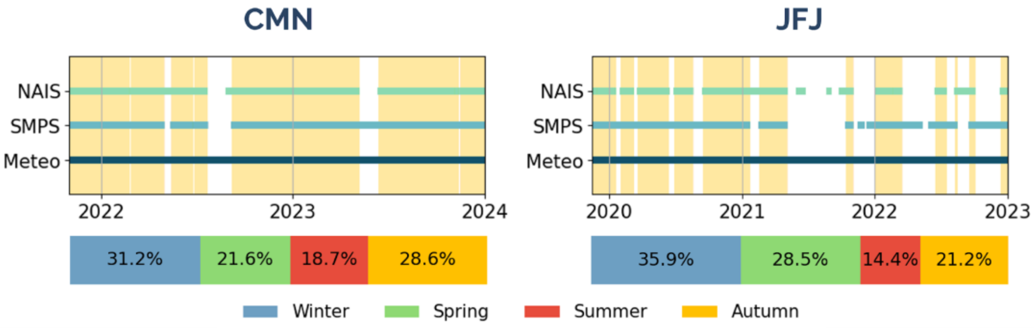

Figure S1. Data coverage at CMN and JFJ for NAIS, SMPS, and meteorological data. The yellow area indicates the common operational period for both NAIS and SMPS at each station. The percentage coverage by seasons refers to these overlapping measurement periods.

S2 Sensitivity analysis of scaling applied to NAIS–SMPS harmonization

A quantitative sensitivity analysis was performed to assess how particle number concentrations depend on both the magnitude of the applied scaling factor and the size range used to derive it. The scaling configuration adopted in the paper, based on the most stable NAIS–SMPS overlap range (30–40 nm at JFJ and 20–30 nm at CMN), was used as the baseline scenario. The impact of the scaling and the resulting NAIS–SMPS merging on the median particle number size distributions is illustrated in Fig. S2, which shows the individual NAIS and SMPS PNSDs together with the final merged distributions. In the merged datasets, NAIS-derived concentrations are used below the merging diameters (35 nm at JFJ and 25 nm at CMN), while SMPS data dominate at larger sizes. The resulting mean scaling factors were 3.38 ± 2.05 for CMN and 3.18 ± 2.07 for JFJ.

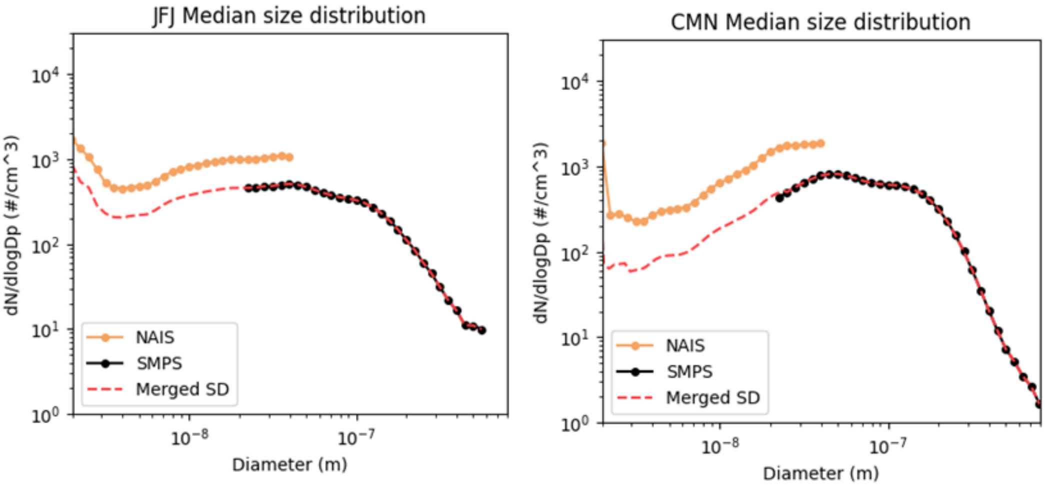

Figure S2. Median PNSD derived by NAIS and SMPS instruments at JFJ and CMN stations. The red dotted line represents the final merged PNSD, after NAIS data correction.

The baseline results were compared with two alternative configurations: (i) a case without any scaling, in which uncorrected NAIS data were used below 25 nm at CMN and 35 nm at JFJ, and (ii) cases using stronger scaling factors derived from smaller overlap ranges (10–20 nm at CMN and 20–30 nm at JFJ). The resulting mean and median particle number concentrations for all size modes and scaling scenarios are summarized in Table S1.

At JFJ, particle number concentrations in the NAIS-only size range show a strong dependence on the applied scaling. In the intermediate mode $N_{2.5-7}$, the mean concentration increases from 379.5 cm^{-3} in the baseline case to 789.6 cm^{-3} without scaling (+108%), while the median increases from 91.5 cm^{-3} to 248.4 cm^{-3} (+171%). Applying a stronger scaling factor derived from the 20–30 nm overlap range (4.63 ± 3.56) reduces the mean concentration to 234.9 cm^{-3} (−38%) and the median to 67.7 cm^{-3} (−26%). A comparable sensitivity is observed in the nucleation mode N_{7-25}, where the mean varies by +130% (without scaling) and −34% (stronger scaling) relative to the baseline. In the Aitken N_{25-100} range, which is partially constrained by SMPS data, the mean changes by +33% and −3%, respectively.

At CMN, removing the scaling increases the mean concentration of particles in the intermediate mode $N_{2.5-7}$ from 273.5 cm^{-3} to 864.1 cm^{-3} (+216%) and the median from 65.0 cm^{-3} to 188.2 cm^{-3} (+189%). Applying a stronger scaling factor derived from the 10–20 nm overlap range (6.97 ± 15.54) reduces the mean concentration to 209.4 cm^{-3} (−23%) and the median to 54.8 cm^{-3} (−16%) relative to the baseline.

	JFJ [cm^{-3}]					**CMN [cm^{-3}]**				
	$N_{2.5-7}$	N_{7-25}	N_{25-100}	$N_{100-500}$	N_{2-500}	$N_{2.5-7}$	N_{7-25}	N_{25-100}	$N_{100-500}$	N_{2-500}
	Baseline Scaling (30–40 nm)					**Baseline Scaling (20–30 nm)**				
Mean	379.5	442.1	336.1	165.9	1323.6	273.5	546	665	302.2	1786.6
Median	91.5	197.3	222.4	68.6	770.2	65	220.2	443.2	176.2	1218.9
SD	1654.2	993.3	384.7	234.6	2387.3	909.4	1179.8	777.4	322.7	2252.3
P25	41.2	96.4	126.6	32.8	482.7	27.6	100.5	253.1	60.3	733.5
P75	231.9	424.7	404.1	177.7	1444.6	182.6	525.8	776.5	449.2	2029
	No Scaling					**No Scaling**				
Mean	789.6	1016.1	448.5	165.9	2418.7	864.1	1592.3	665	302.2	3646
Median	248.4	515.8	295.4	68.6	1404.3	188.2	633.8	443.2	176.2	2101.2
SD	2348.8	2051.9	497	234.6	3891.6	3067.2	4838.3	777.4	322.7	7475.9
P25	128.5	297.5	174.2	32.8	898.7	87.9	327.3	253.1	60.3	1248.3
P75	549	974.7	538.3	177.7	2505.8	512.2	1483.7	776.5	449.2	3830.6
	Scaling (20-30 nm)					**Scaling (10-20 nm)**				
Mean	234.9	292.8	327.2	165.9	1021.2	209.4	420.4	665	302.2	1595.9
Median	67.7	135.1	214.7	68.6	634.1	54.8	159.5	443.2	176.2	1039.7
SD	908.2	618.5	377.1	234.6	1510.4	1044.9	971	777.4	322.7	2138.5
P25	29.9	63.8	122	32.8	389.1	22.8	76.7	253.1	60.3	624.1
P75	166.2	295	391.6	177.7	1199.4	138.7	356.9	776.5	449.2	1806

Table S1. Mean, median, standard deviation (SD) and percentiles (P25, P75) of particle number concentrations (cm^{-3}) for different size ranges at JFJ and CMN under alternative NAIS–SMPS scaling configurations.

Overall, the sensitivity analysis demonstrates that particle number concentrations below the merging diameters are sensitive to both the magnitude of the applied scaling factor and the size range used to derive it. When expressed as fractional contributions, the relative partitioning between the intermediate and nucleation modes varies depending on whether scaling is applied. However, the combined contribution of small particles (2.5–25 nm) remains consistently higher at JFJ than at CMN for both the scaled and unscaled datasets, while CMN remains dominated by the Aitken and accumulation modes. Seasonal and diurnal variability patterns, as well as the relative ordering of particle size modes and the site-to-site contrasts, are preserved across all tested scaling scenarios. Consequently, uncertainties associated with the harmonization procedure propagate predominantly into the smallest size classes and affect absolute concentrations and derived quantitative metrics, while the qualitative conclusions presented in the main text remain robust to reasonable variations in the scaling assumptions.

S3 Calculation of Growth and Formation Rates, Coagulation and Condensation Sink

To characterize NPF events, we calculated both the particle formation rate J and the growth rate GR for particles within the 2.5–7 nm size range. The formation rate $J_{2.5}$ represents the flux of particles growing beyond the 2.5 nm threshold and was determined based on the aerosol general dynamic equation (Kulmala et al., 2012). This equation accounts for the time-dependent change in particle number concentration and includes terms for both coagulation losses and particle growth:

$$J_{2.5} = \frac{dN_{2.5,7}}{dt} + CoagS_{2.5-7} \cdot N_{2.5-7} + \frac{GR_{2.5-7}}{(7-2.5)nm} \cdot N_{2.5-7}$$

In this formulation, $N_{2.5-7}$ is the concentration of particles between 2.5 and 7 nm, $CoagS_{2.5-7}$ represents the coagulation sink for this size range, and $GR_{2.5-7}$ denotes the growth rate of the particles.

The coagulation sink describes the rate at which particles are lost due to coagulation with other particles, effectively removing them from the nucleation mode. It is calculated by integrating over all particle size bins and considering the collision rates between particles of different sizes. The coagulation sink $CoagS(d_p)$ for a given particle diameter d_p is defined as:

$$CoagS(d_p) = \sum_{d_{p_i} \geq d_p} K\left(d_p, d_{p_i}\right) \cdot N\left(d_{p_i}\right) \cdot \Delta d_{p_i}$$

where $K\left(d_p, d_{p_i}\right)$ is the coagulation coefficient between diameters d_p and d_{p_i}, $N\left(d_{p_i}\right)$ is the number concentration of particles with diameter d_{p_i}, and Δd_{p_i} is the differential diameter.

The average coagulation sink $\langle CoagS \rangle_{2.5-7}$ for diameters between 2.5 and 7 nm was calculated as:

$$\langle CoagS \rangle_{2.5-7} = \frac{1}{N} \sum_{d_p \in [2.5nm, 7nm]} CoagS(d_p)$$

where N is the number of diameters d_p considered within the range of 2.5 and 7 nm.

The $GR_{2.5-7}$ was determined using the maximum concentration method (Kulmala et al., 2012), which identifies the time at which the peak particle concentration occurs. First, the particle size distribution data were smoothed using a rolling median filter and further refined using a Gaussian filter to reduce noise. This allowed for accurate detection of the time of maximum concentration for particles within the 2.5 and 7 nm size range. These time points were then plotted against the corresponding particle diameters, and a linear least-squares fit was applied to the data. The slope of this line was used to calculate the $GR_{2.5-7}$:

$$GR_{2.5-7} = \frac{\Delta d_{p_{[2.5-7]}}}{\Delta t}$$

where $\Delta d_{p_{[2.5-7]}}$ is the change in particle diameter (from 2.5 to 7 nm), and Δt is the corresponding time interval. The GR, expressed in nm/h, provides a measure of how quickly particles grow during NPF events. The growth rate was a value retrieved only for the day of new particle formation events, one for each nucleation day.

In addition to the coagulation sink, the condensation sink CS was also considered, which quantifies the rate at which condensing vapors, such as sulfuric acid, are scavenged by the pre-existing aerosol population. This is an important factor as it influences the availability of condensable vapors that drive particle growth. The CS is calculated as (Kulmala et al., 2012):

$$CS = 4\pi D \sum_i (N_i \cdot \beta\left(d_{p_i}, T, P, D, M_{H_2SO_4}\right) \cdot d_{p_i})$$

where D is the diffusion coefficient of the condensing vapor, which we consider to be sulfuric acid in air, N_i is the number concentration of aerosol particles, d_{p_i} is the particle diameter, and β is the deposition coefficient. The number concentration is derived from the aerosol number size distribution, and the binary diffusivity and deposition coefficients are determined based on the ambient conditions. The summation is performed over all diameter bins of the aerosol size distribution.

S4 PNSD seasonality

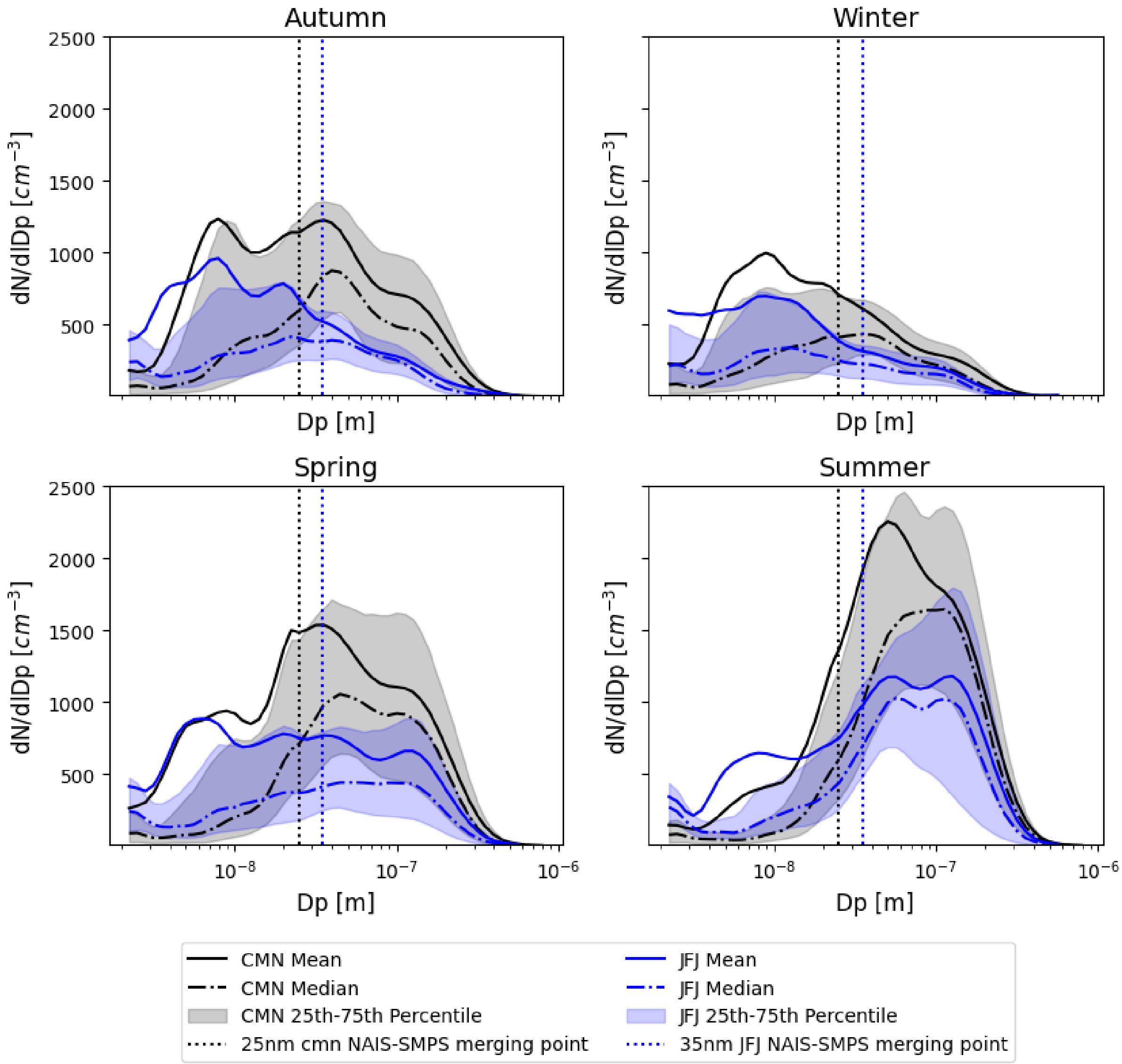

Figure S3. Seasonal variation of particle size distribution at the CMN (black) and JFJ (blue) stations. The dashdotted lines represent the median, while the solid lines indicate the mean particle size distribution. The shaded area encompasses the interquartile range, reflecting the 25th to 75th percentiles. The vertical dashed lines mark the merging points between the scaled NAIS size distribution and the SMPS size distribution (25 nm at CMN and 35 nm at JFJ).

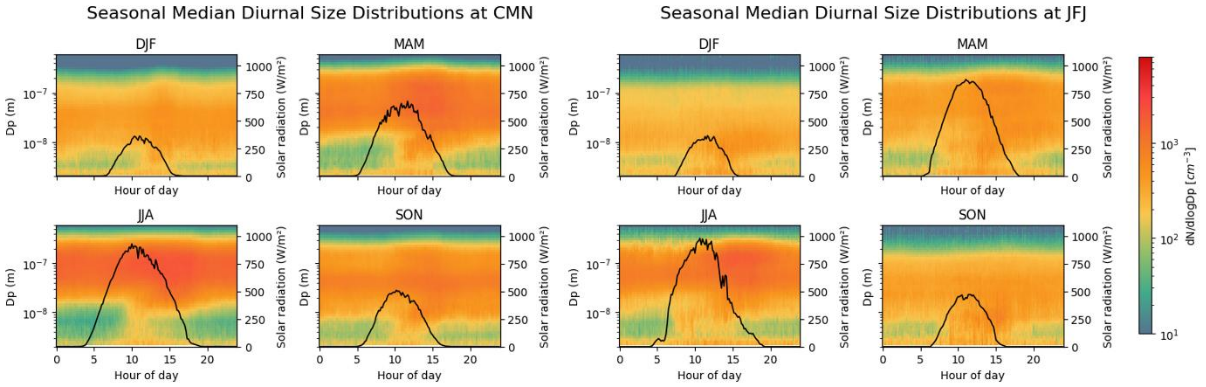

Figure S4. Seasonal median diurnal aerosol size distributions at CMN (left column) and JFJ (right column). Each panel shows the median particle number size distribution as a function of hour of day (10-minute resolution) and particle diameter (Dp), derived from NAIS and SMPS combined measurements and displayed using a logarithmic dN/dlogDp color scale. Across all seasons (DJF, MAM, JJA, and SON) the overlaid black line illustrates the corresponding seasonal median diurnal cycle of global solar radiation (right-hand axis).

S5 Ions Seasonal diurnals

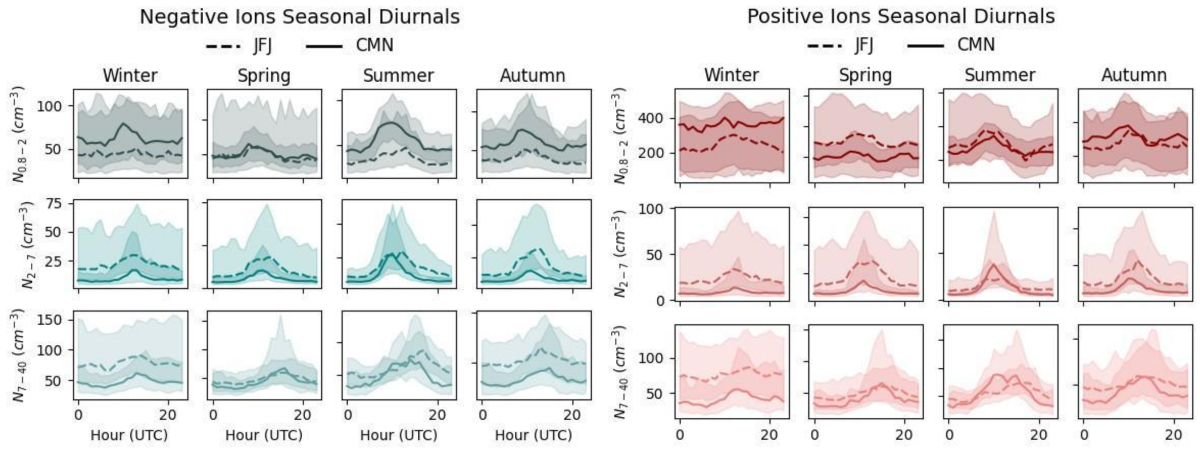

Figure S5. Diurnal variation of negative (left) and positive (right) number concentrations across three modes (0.8–2 nm, 2–7 nm and 7–40 nm) for each season at the CMN and JFJ stations. All times are in UTC.

The diurnal behaviour of the ions is similar at both stations as shown in Fig. S3. At JFJ, the negative cluster ions exhibit peak activity predominantly in the early afternoon, around 13:00 to 14:00, during the winter and summer seasons. During spring and autumn, the peak occurs earlier, at around 12:00. Negative intermediate ions follow a similar pattern, maintaining consistent peak times around midday, generally between 12:00 and 13:00, with minor seasonal shifts. However, negative large ions show a tendency to peak later in the afternoon, especially in spring and summer, where their peak times extend from 14:00 to as late as 17:00. Positive cluster ions closely follow the diurnal pattern of negative cluster ions, peaking between 12:00 and 14:00 in most seasons, except for autumn, when the peak occurs at 10:00. Meanwhile, positive intermediate and large ions display more delayed peak times, particularly for the latter, where the maximum is observed as late as 16:00 during spring and summer.

At CMN, the diurnal behavior of ions shifts to earlier hours compared to JFJ. Negative cluster ions peak between 08:00 and 10:00 during most seasons. Negative intermediate ions peaks also occur at earlier hours, after the maximum cluster ions peaks, between 10:00 and 12:00. Finally, large negative ions at CMN display a tendency to peak in the early to mid-afternoon, from 13:00 to 16:00, with particularly delayed peaks in spring and autumn. The behavior of positive cluster ions is like that of negative cluster ions, except the large positive ions that typically reach their maximum later in the day, between 13:00 and 15:00.

S6 In-Cloud Conditions and Particle Size Distribution

A closer examination of the particle size distribution when RH exceeds 97% shows an anomalous increase in sub-10 nm particles (Fig. S4), the origin of which remains uncertain. Further investigation is needed to determine whether this signal reflects a real atmospheric process or an instrumental artifact. At the same time we can see clearly how in-cloud scavenging is responsible for the observed decrease in CCN (50–800 nm).

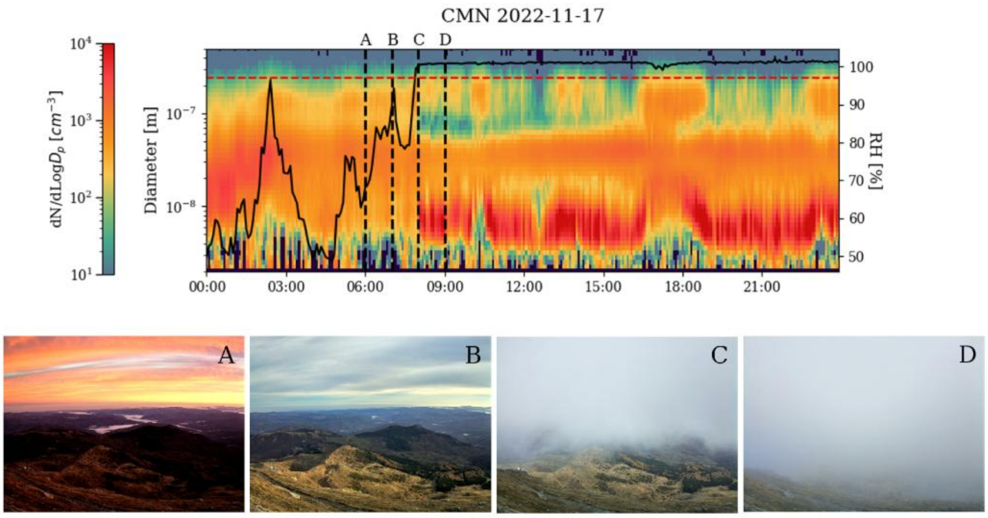

Figure S6. Case study from 2022-11-17 at CMN. The solid black line represents the relative humidity (RH) variation throughout the day, while the red dotted line marks the 97% RH threshold, above which the station is considered to be in cloud. Points A, B, C, and D correspond to 6:00, 7:00, 8:00, and 9:00, respectively, illustrating the transition from out-of-cloud to in-cloud conditions, as observed via the station's weather camera.

S7 NPF event frequency across classification methods

	Class IA	Class IB	Class II	Not Event	Undefined
CMN	9.3%	12.4%	10.2%	61.2%	7.0%
JFJ	2.7%	4.9%	5.8%	50.0%	36.6%

Table S2. Event statistics at CMN and JFJ according to Dal Maso et al. (2005) classification.

	Regional	Transported	Bursts	Not Event
CMN	22.3%	13.3%	14.0%	50.3%
JFJ	3.8%	9.8%	15.0%	71.4%

Table S3. Event statistics at CMN and JFJ according to Dada et al. (2017) classification.

	Intense	Moderate	Weak	Negligible
CMN	11.0%	17.4%	30.8%	40.9%
JFJ	4.6%	12.8%	31.5%	51.2%

Table S4. Event statistics at CMN and JFJ according to Nanoparticle ranking analysis (Aliaga et al., 2023).

S8 Diurnal Meteorological Patterns on Intense vs. Negligible NPF Days

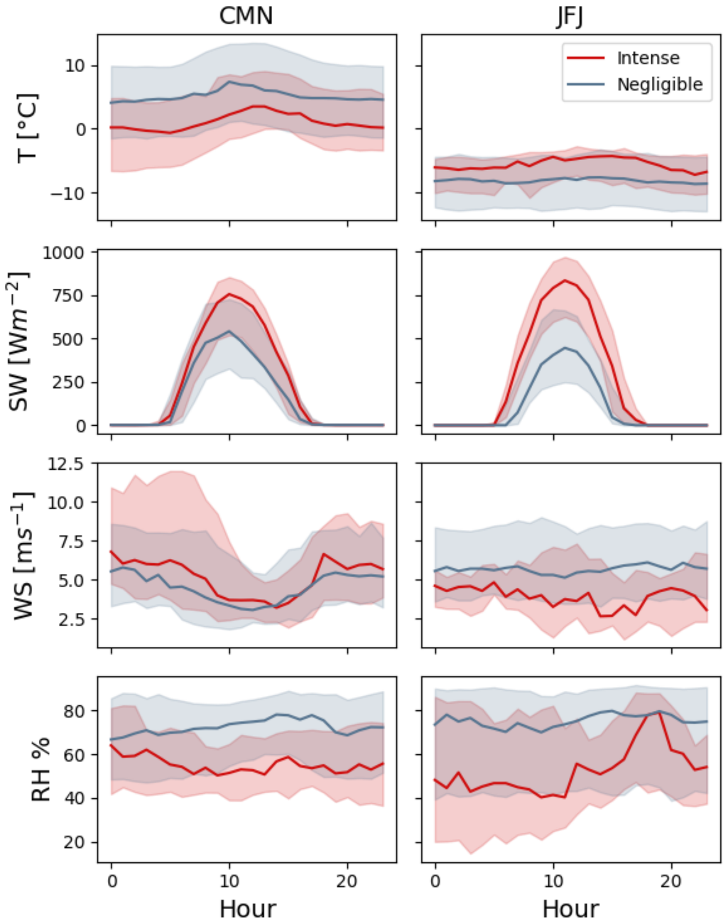

Figure S7. Comparison of median diurnal meteorological conditions between intense NPF days (red) and negligible NPF days (blue) at CMN (left column) and JFJ (right column). For each subset of days, the solid lines represent the hourly median and the shaded envelopes indicate the interquartile variability (25th–75th percentiles). From top to bottom, panels show air temperature (T), incoming shortwave radiation (SW), wind speed (WS), and relative humidity (RH). The figure illustrates systematic meteorological differences associated with days exhibiting strong new particle formation, including enhanced daytime shortwave radiation, distinct temperature evolution, and characteristic changes in wind and humidity patterns relative to days with negligible NPF activity.